Inorganic Chemistry

Article

pubs.acs.org/IC

Interlayer Switching of Reduction in Layered Oxide, $Bi_4V_2O_{11-\delta}$ ($0 \leq \delta \leq 1$)

Yaoqing Zhang* and Yutaka Ueda

Institute for Solid State Physics, The University of Tokyo, Kashiwanoha 5-1-5, Kashiwa, Chiba 277-8581, Japan

Supporting Information

ABSTRACT: In contrast to the rich oxygen nonstoichiometry in vanadium oxides, we report here an interesting $Bi_4V_2O_{11-\delta}$ oxide system whose vanadate layer allows only a narrow oxygen deficiency range. Beyond $\delta = 0.4$, reduction of $Bi_4V_2O_{11-\delta}$ does not proceed in the V−O layer, but instead suddenly switches to the Bi−O layer by precipitation of metallic bismuth. A new structure is realized for $0.4 \leq \delta \leq 1$, and its ordered V^{4+} cation forms a rigid $V^{4+}/V^{5+} = 2/3$ pair giving rise to one-dimensional magnetism that can be understood in terms of an $S = {}^1/_2$ antiferromagnetic Heisenberg chain model. In situ X-ray diffraction measurement yielded the first phase diagram for the system of current study and revealed the unusual phase relation as a function of oxygen nonstoichiometry. It is suggested that at higher temperatures than 570 °C all compositions would be unified into an oxygen disordered tetragonal phase, whose implication for oxide ion mobility could have significant impact on our understanding of ionic conduction.

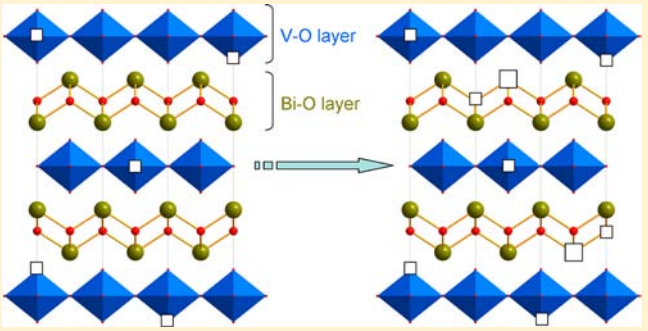

1. INTRODUCTION

The pseudo binary oxide system Bi_2O_3-V_2O_5 has received considerable interest because of its wide structural diversity and rich functional properties.[1−5] Of particular interest is the tetrabismuth divanadium oxide phase $Bi_4V_2O_{11}$ which is found exhibiting remarkably high oxygen anionic mobility.[6−8] Such a function promises serious potential applications in many important areas, for example, solid oxide fuel/electrolysis cells[9,10] and oxygen sensors.[11] The crystal structure of idealized $Bi_4V_2O_{11}$, as shown in Figure 1, is thought to be closely related to the Aurivillius form, which is built up from infinite $(Bi_2O_2)^{2+}$ sheets sandwiched between oxygen deficient $VO_{4-\Delta}$ perovskite slabs (V−O layer), giving a unit cell of $a_p \times b_p \times 4c_p$, where a_p, b_p, and c_p represent the simple perovskite lattice constants.[12−14] In $(Bi_2O_2)^{2+}$ sheets, Bi takes a square pyramidal coordination by sitting above and below oxygen planar squares alternatively with its $6s^2$ lone pair orbitals pointing to vacant positions between corners of adjacent perovskite units. Intrinsic oxygen vacancies ($\Delta = 0.5$) in the V−O layer, which is normally believed to enable high oxide ion conductivity, are located in both apical and equatorial sites of VO_6 octahedra randomly. Such a description represents a widely accepted prototype structure for the high temperature γ-phase ($a_p = b_p$).[13,14] With decreasing temperature, $Bi_4V_2O_{11}$ undergoes two consecutive and reversible phase transitions, $\gamma \rightarrow \beta$ and $\beta \rightarrow \alpha$ at 553 °C (575 °C for $\beta \rightarrow \gamma$) and 386 °C (440 °C for $\alpha \rightarrow \beta$), respectively, because of the long-range oxygen vacancy ordering process (see Supporting Information, Figure S1). The β-phase crystallizes in an orthorhombic lattice whose unit cell is characterized by a 2-fold superstructure and can be related to the γ-phase through a simple relation: $a_\beta = 2\sqrt{2}a_\gamma$, $b_\beta = \sqrt{2}b_\gamma$, $c_\beta = c_\gamma$.[15] The β-structure is thought to involve a building unit consisting of a V−O trigonal bipyramid and two corner-sharing tetrahedra, which extends along [110] and [1$\bar{1}$0] directions. The ambient stable α-polymorph reveals a commensurate superstructure that triples the a-axis of an orthorhombic "mean cell", leading to a further larger cell volume, $a_\alpha = 3\sqrt{2}a_\gamma$, $b_\alpha = \sqrt{2}b_\gamma$, $c_\alpha = c_\gamma$.[6,15] The α-phase retains the orthorhombic symmetry despite a few different reports claiming their observation of the monoclinic distortion.[16] Unfortunately, because of the complexity, its exact crystal structure is not fully understood yet. The key stumbling block in picturing a plausible structural model is that, in practice $Bi_4V_2O_{11}$ free from $BiVO_4$ impurity seems very difficult or impossible to be synthesized from stoichiometric Bi_2O_3 and V_2O_5 precursors through the traditional solid state reaction method.[15−19] Instead, it was suggested that derivative $Bi_4V_2O_{11-\delta}$ could be prepared in a single phase.[17,18]

The oxygen-vacancy-disordered γ-phase reminds us that there might exist a rich phase diagram in the oxygen deficient system where a wealth of unknown phases would be expected. In fact, there have been a few reports over possible compositions in the $Bi_4V_2O_{11-\delta}$ series including $\delta = 0.33$ and 1. According to Joubert et al., samples synthesized in an atmosphere of 10%H_2/Ar yielded $Bi_4V_2O_{10.66}$, which means only one-third of the vanadium could be reduced, hence leading to a mixed valence of $V^{4+}/V^{5+} = 1/2$.[20] The subsequent X-ray powder diffraction analysis revealed that the crystal structure of

Received: January 16, 2013
Published: April 15, 2013

   dx.doi.org/10.1021/ic400111w | Inorg. Chem. 2013, 52, 5206−5213

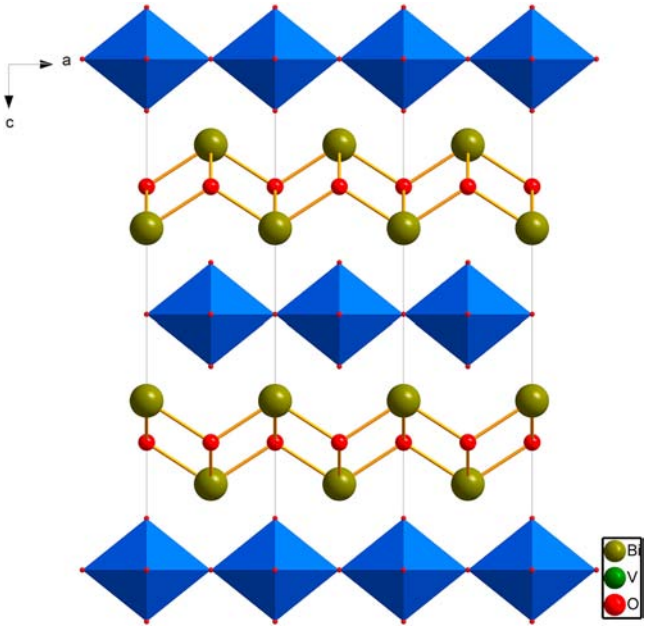

Figure 1. Schematic diagram of γ-$Bi_4V_2O_{11}$ structure viewed down the b axis. The oxygen deficient $VO_{4-\Delta}$ perovskite layer is highlighted in blue for clarity, and the Bi_2O_2 sheet consists of a planar square array of oxygen with Bi^{3+} cations sitting above and below alternately.

$Bi_4V_2O_{10.66}$ at room temperature is different from $Bi_4V_2O_{11}$. It was further demonstrated that a 3-fold commensurate modulation is also developed in $Bi_4V_2O_{10.66}$ but along the b-axis ($a < b$) in the form of $\sqrt{2}a_p \times 3\sqrt{2}b_p \times 4c_p$, whereas the same 3-fold superstructure is formed along the a-axis in the case of α-$Bi_4V_2O_{11}$. The structural model proposed then based on synchrotron X-ray diffraction (XRD) data to account for the tripled unit cell is to view the composition of the V−O layer as $(V_3O_{10})^{6-}$ ribbons which include $V^{4+}O_6$ octahedra and $V^{5+}O_4$ tetrahedra with the ratio of 1 to 2. This model is quite reasonable; however, as pointed out in the original document, impurity-free $Bi_4V_2O_{10.66}$ was not achieved either, indicative of a possibility of a small departure in the real composition or an important role that the defect chemistry has played. Against the reduction limit mentioned above, Satto and Millan et al. recently reported a success in identifying a new member material $Bi_4V_2O_{10}$ in which V^{5+} is fully replaced by V^{4+}.[21,22] The authors further suggested that the vanadium layer in this compound is built up simply by corner-sharing VO_5 square pyramids in an ordered manner with a unit cell of $\sqrt{2}a_p \times 3\sqrt{2}b_p \times 4c_p$ which is the same as that of $Bi_4V_2O_{10.66}$. However, this does not seem to be the case. Apparently, the failure to take the constant presence of metallic bismuth into account jeopardizes the reliability of their conclusions.

To bridge the gap between those very scattered results and the real compositional diversity in $Bi_4V_2O_{11-\delta}$, a detailed study of the structural phase diagram is of significance and thus required, in particular for a deep understanding of the structural dependence on composition as well as temperature in this system. In addition to significance to crystal chemistry, defect chemistry, nonstoichiometry, and bismuth chemistry, the function of high oxygen anionic mobility is also appealing in $Bi_4V_2O_{11-\delta}$ whose larger number of intrinsic vacant oxygen sites could facilitate higher oxide ion conductivity than the parent phase.

Moreover, $Bi_4V_2O_{11-\delta}$ is of particular interest as the two-dimensional square lattice enables Aurivillius a favored structure carrier of novel quantum properties.[23,24] In response to decreasing oxygen contents the expanding share of the d^1 cation V^{4+} could further yield vanadium sublattices with an ordered fashion between V^{4+} and V^{5+}. Information on how the magnetic interaction aligns adjacent moments is useful to not only illustrate the accurate structure but also offer fresh insight into the low dimensional magnets. On the other hand, carrier doping into layered $VO_{4-\Delta}$ perovskite slabs by reduction may produce interesting electronic properties as is the cases of high T_c cuprates[25] and iron based superconductors.[26]

In this contribution we take a comprehensive approach by scrutinizing the full spectrum of the δ value in $Bi_4V_2O_{11-\delta}$ ($0 \leq$

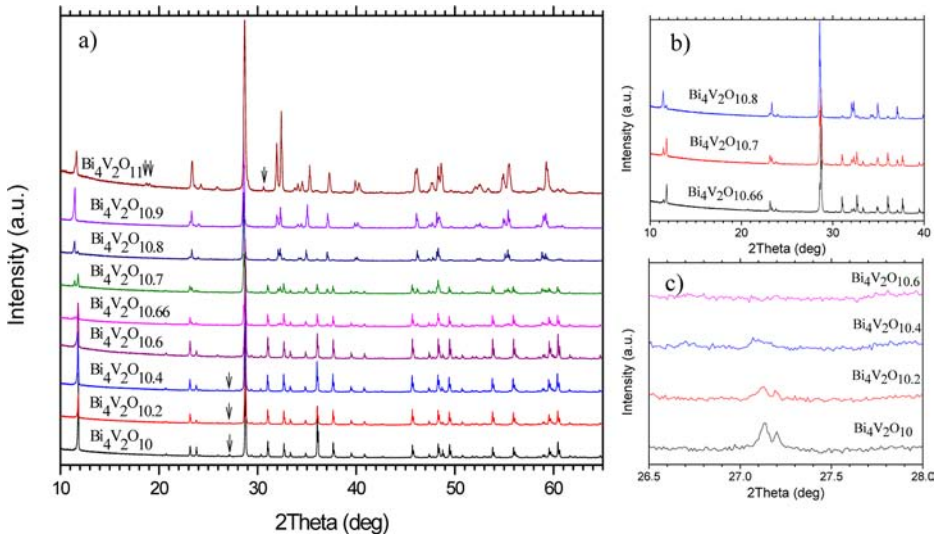

Figure 2. (a) Room temperature XRD patterns for representative compositions in $Bi_4V_2O_{11-\delta}$ ($0 \leq \delta \leq 1$). For the sake of a better comparison, all samples were synthesized at 600 °C simultaneously except $Bi_4V_2O_{11}$ which was prepared separately at 800 °C in flowing oxygen atmosphere. (b) Two phase mixture region for $0.4 < \delta < 0.1$ where patterns for two types of structure coexist (δ = 0.2, 0.3, and 0.33 from top to bottom). (c) The bismuth impurity dependence on composition (δ = 0.4, 0.6, 0.8, and 1 from top to bottom) by enlarging the strongest diffraction peak for bismuth.

dx.doi.org/10.1021/ic400111w | Inorg. Chem. 2013, 52, 5206−5213

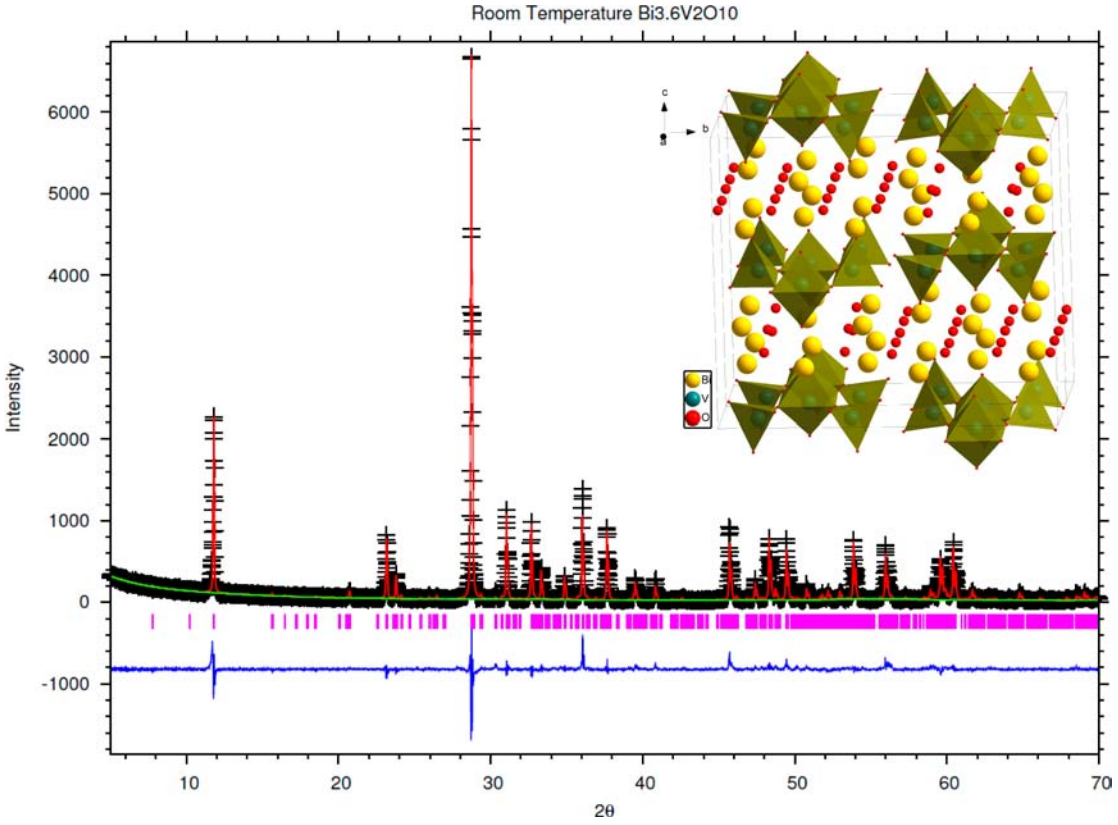

Figure 3. Rietveld refinement profile of room temperature XRD data for $Bi_{3.6}V_2O_{10}$ synthesized at 600 °C. Observed data, calculated pattern, and the difference profile are shown as cross sign (black), solid line (red), and continuous line (blue). The tick marks show the position of Bragg reflections predicted by the structural model while the green line is to reproduce the background. Inset shows the 3-dimensional view of the atomic structure for A-type $Bi_{3.6}V_2O_{10}$.

$\delta \leq 1$) and show clearly for the first time how materials evolve with varying oxygen deficiency.

2. EXPERIMENTAL PROCEDURES

2.1. Materials Synthesis. Polycrystalline samples of $Bi_4V_2O_{11-\delta}$ ($0 < \delta \leq 1$) were synthesized via a conventional solid state reaction method using Bi_2O_3 (Rare Metallic, 99.999%), V_2O_3 (Rare Metallic, 99.9%), and V_2O_5 (Rare Metallic, 99.999%) with stoichiometric ratio as starting materials. After thoroughly being ground, the precursor mixtures were pelletized and sealed into a quartz tube under vacuum of some 10^{-3} mbar. Pellets were then heated at 600 °C for 72 h before cooled down to room temperature at a rate of 5 °C min^{-1}. Only Bi_2O_3 and V_2O_5 (2:1) were used for the synthesis of $Bi_4V_2O_{11}$ by heating at 800 °C with flowing oxygen gas for 48 h with an intermediate grinding step. Bismuth deficient samples, $Bi_{4-x}V_2O_{10}$ and $Bi_{3.87}V_2O_{10.4}$, were synthesized from stoichiometric Bi_2O_3, V_2O_3 and V_2O_5 precursors according to the same procedure for $Bi_4V_2O_{11-\delta}$.

2.2. TG-DTA. Thermal gravimetric analysis (TGA) and differential thermal analysis (DTA) were carried out on MAC Science 2000S instrument to evaluate the oxygen gain and the enthalpy change. The measurements were done in the range of 30−800 °C at heating/cooling rate of 10 °C/min under air for $Bi_4V_2O_{11}$ powder. For $Bi_4V_2O_{10.6}$, powder sample is sealed into a special quartz vessel with very thin bottom under vacuum of 10^{-3} mbar to avoid sample oxidization during the measurements.

2.3. In Situ and Ex Situ XRD. Room temperature ex situ XRD data of as-prepared polycrystalline samples were collected on a Rigaku Smartlab diffractometer with CuK_α radiation source and a position-sensitive detector. The step size was set to be 0.01°. In situ high temperature structural characterization was performed on a MAC Science MXP-18 diffractometer with CuK_α radiation, equipped with a furnace. The sample was sealed in an evacuated silica capillary with a diameter of 1.5 mm and wall-thickness of 0.01 mm to avoid sample oxidization during the measurements. The step size was set to 0.02°, and each step was scanned for 10 s.

2.4. Magnetic Susceptibility. Magnetic susceptibility was measured by a superconducting quantum interface device (SQUID Quantum Design MPMS-5S) magnetometer for 1.8−300 K in both zero field cooling (ZFC) and field cooling (FC) modes under a magnetic field of 50 kOe.

3. RESULTS AND DISCUSSION

3.1. Phase Relation at Room Temperature. To examine the evolution of the crystal structure of the $Bi_4V_2O_{11-\delta}$ system as a function of the oxygen content, a reasonably broad range of compositions with $0 \leq \delta \leq 1$ were synthesized simultaneously at 600 °C, except $Bi_4V_2O_{11}$ which was synthesized separately at 800 °C with flowing oxygen gas. According to the room temperature XRD patterns as shown in Figure 2a, all examined phases are found to be generally associated with two distinct structural types. The first one is closely related to $Bi_4V_2O_{11}$, or strictly α-$Bi_4V_2O_{11}$. Consistent with previous studies, α-$Bi_4V_2O_{11}$ is indeed not immune from the $BiVO_4$ pollution whose presence is marked by arrows at positions of the main peak (Figure 2a), although the current synthesis has been optimized by utilizing an oxygen rich atmosphere. Surprisingly, single phased $Bi_4V_2O_{10.9}$ in the present work is obtained and reveals itself clearly to be a member of this structural family. All strong peaks in the XRD profile for $Bi_4V_2O_{10.9}$ can be readily indexed into an orthorhombic unit cell, $\sqrt{2}a_p \times \sqrt{2}b_p \times 4c_p$. Besides, evidenced in Figure 2a, several extra reflections can be also observed in the low angle range from 23 to 35°, indicating

dx.doi.org/10.1021/ic400111w | Inorg. Chem. 2013, 52, 5206−5213

the appearance of superstructure, and a supercell of $3\sqrt{2}a_p \times \sqrt{2}b_p \times 4c_p$ has to be used to account for the actual unit cell parameters. This is completely in agreement with the case of α-$Bi_4V_2O_{11}$.

Another structural type, demonstrated by the sharply different XRD profile from that of the first type, appears clearly from $Bi_4V_2O_{10.6}$ and is retained across the whole range of δ values from 0.4 to 1. Take $Bi_4V_2O_{10.6}$ for instance, this single phased composition crystallizes in an orthorhombic symmetry as well; however, its unit cell becomes $\sqrt{2}a_p \times 3\sqrt{2}b_p \times 4c_p$ where the b-axis instead of the a-axis is tripled compared to α-$Bi_4V_2O_{11}$ type. Hereafter we refer to this structure as A-type. Compositions between $Bi_4V_2O_{10.6}$ and $Bi_4V_2O_{10.9}$ fall into a two-phase mixture region where two structural types (α- and A-type) coexist and compete with each other, as the relative fraction of both phases depends on δ. In Figure 2b, XRD patterns for both $Bi_4V_2O_{10.8}$ and $Bi_4V_2O_{10.7}$ precisely show the presence of characteristic reflections from both structures. What is particularly worth noting is that the widely studied compound $Bi_4V_2O_{10.66}$ does not exist as an individual phase but proves to be also a member material in the mixture regime. Instead, we can isolate $Bi_4V_2O_{10.6}$ as a single phased product that becomes the first compound in the $Bi_4V_2O_{11-\delta}$ series to adopt the second type structure (A-type).

The α-$Bi_4V_2O_{11}$ typed structure is tolerated only as far as δ = 0.1, although a slight shift could be anticipated to the real phase boundary as the compositional step was only limited to 0.1. In contrast, $Bi_4V_2O_{11-\delta}$ ($0.4 \le \delta \le 1$) survives as an isostructural system despite the much wider compositional range. Again in Figure 2a, if looking into the patterns in detail, we can easily see that toward the oxygen poor side of the phase diagram, there is actually a progressive appearance of the extra weak diffraction lines that are responsible for the only impurity of metallic bismuth, coupled with a gradual intensity enhancement. The arrows in Figure 2a locate the position of the main peak corresponding to metallic bismuth, and Figure 2c shows enlarged patterns for better visualization. This finding is significant as it suggests, on the one hand, that the only single phase lies at δ = 0.4. On the other hand, more importantly the precipitation of metallic bismuth from the host material strictly implies the presence of bismuth vacancies and thus oxygen vacancies in the Bi_2O_2 fluorite-like layers (Bi−O layer). One can thus reasonably anticipate the prevailing composition of $Bi_4V_2O_{11-\delta}$ to be $Bi_{4-x}V_2O_{11-\delta}$ for $\delta > 0.4$. By use of energy-dispersive X-ray spectroscopy (EDX), we obtained a real composition of $Bi_{3.6}V_2O_{10}$ for nominal $Bi_4V_2O_{10}$. To further confirm the real composition $Bi_{3.6}V_2O_{10}$, we prepared $Bi_{4-x}V_2O_{10}$ ($0 \le x \le 1$) and characterized it by XRD. The compounds with $x < 0.4$ contain metallic bismuth, while in $x > 0.4$ $BiVO_4$ appears as an impurity instead of metallic bismuth. In Figure 3 we present the corresponding XRD pattern for $Bi_{3.6}V_2O_{10}$ and its Rietveld fitting using the GSAS-EXPGUI package.[27,28] No impurity particularly metallic bismuth could be detected within the same experimental resolution as that in Figure 2a. Instead, with a starting model for $Bi_4V_2O_{10.66}$ our refinement (χ^2 = 2.467) yielded a clear deficiency at the bismuth site that is 10.375% or $Bi_{3.585}$ and generally agrees with our synthesis observation of 10% or $Bi_{3.6}$ (see Supporting Information, Table S1). It means the bismuth cationic vacancies in $Bi_{3.6}V_2O_{10}$ could not be due to the presence of any amorphous vanadium rich phases but intrinsic. A-type $Bi_{3.6}V_2O_{10}$ proves to be an oxygen ordered phase with an orthorhombic $\sqrt{2}a_p \times 3\sqrt{2}b_p \times 4c_p$ supercell (a = 5.467322; b = 17.236130; c = 14.917385 Å). According to the refinement, the supercell of A-$Bi_{3.6}V_2O_{10}$ contains octahedrally coordinated tetravalent vanadium ions as well as tetrahedrally coordinated pentavalent vanadium cations. The former $V^{4+}O_6$ units arrange themselves in a linear manner and are stacked alternatively with every two $V^{5+}O_4$ tetrahedron chains. The vanadate layer structure is thus very close to the idealized phase $Bi_4V_2O_{10.66}$, and its composition can be written as ($VO_{3.3}$), while the bismuthate layer in $Bi_{3.6}V_2O_{10}$, accommodates bismuth vacancies which are found to be randomly distributed at all sites. As an illustration of the A-type crystal structure, a schematic representation is given in the inset to Figure 3. However, it should be noted that the slightly larger molar ratio of V^{4+}/V^{5+} in $Bi_{3.6}V_2O_{10}$ than $Bi_4V_2O_{10.66}$ could cause a local change to the coordination chemistry of vanadium, which however is difficult to be resolved here. What is more intriguing, both $Bi_4V_2O_{10.6}$ and $Bi_{3.6}V_2O_{10}$ are featured by the identical V^{4+}/V^{5+} ratio of 2/3. These results imply that a molar ratio of V^{4+}/V^{5+} = 2/3 is very likely retained across the whole range of compositions with $0.4 \le \delta \le 1$, namely, the relation between bismuth and oxygen deficiencies is expressed as $x = 2\delta/3 - 4/15$ in $Bi_{4-x}V_2O_{11-\delta}$ ($0.4 \le \delta \le 1$). In light of this ratio, we obtained another single phase $Bi_{3.87}V_2O_{10.4}$ (V^{4+}/V^{5+} = 2/3) corresponding to bismuth containing $Bi_4V_2O_{10.4}$. It was also confirmed from magnetic properties that $Bi_{4-x}V_2O_{11-\delta}$ ($0.4 \le \delta \le 1$) have the identical value of V^{4+}/V^{5+} = 2/3 and the same arrangement of V^{4+} and V^{5+}, as described below.

3.2. Magnetic Properties. The A-typed phase possesses an ordered structure as evidenced by the presence of superstructures in its XRD patterns. Further insight into the details of the ordering calls for information of the magnetization behavior for different samples. Figure 4 presents the temperature dependence of magnetic susceptibilities, $\chi(T)$, for $Bi_4V_2O_{10.6}$, $Bi_{3.87}V_2O_{10.4}$, and $Bi_{3.6}V_2O_{10}$ powders, measured between 1.8 and 300 K in both zero field cooled (ZFC) and field cooling (FC) modes with an applied magnetic field of 50 kOe. The $\chi(T)$ curves of the three compounds display a very similar behavior to one another; particularly the $\chi(T)$ curves of

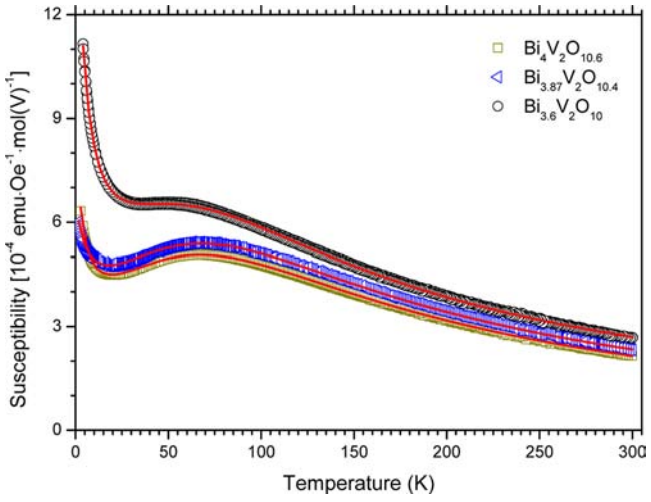

Figure 4. Temperature dependence of magnetic susceptibility in both zero field cooling (ZFC) and field cooling (FC) modes with an applied magnetic field of 50 kOe for $Bi_{3.6}V_2O_{10}$, $Bi_{3.87}V_2O_{10.4}$, and $Bi_4V_2O_{10.6}$ powders. The solid red lines in the figure represent the fit according to an $S = {}^1/_2$ Heisenberg chain model. The error bars are within the size of the symbols used.

dx.doi.org/10.1021/ic400111w | Inorg. Chem. 2013, 52, 5206−5213

$Bi_4V_2O_{10.6}$ and $Bi_{3.87}V_2O_{10.4}$ are almost the same. The notable features of these $\chi(T)$ curves are a broad maximum around 55 K and a Curie tail in the lowest temperature region. Such a broad maximum behavior is characteristic of low dimensional magnetism. In an attempt at quantitative analysis, we applied an $S = {}^1/_2$ Heisenberg one-dimensional (1D) chain model to these $\chi(T)$ curves for a fitting by taking the impurity contribution into account.

$$\chi(T) = \chi_{\mathrm{BiVO}}(T) + \chi_{\mathrm{im}}(T) + \chi_0 = p\frac{Ng^2\mu_B{}^2}{kT}\cdot\frac{A_0 + A_1X^{-1} + A_2X^{-2}}{1 + B_1X^{-1} + B_2X^{-2} + B_3X^{-3}} + \chi_{\mathrm{im}}(T) + \chi_0$$

where $\chi_{\mathrm{BiVO}}(T)$ is the spin part of the compound, $\chi_{\mathrm{im}}(T)$ is the magnetic contribution from the impurity, which gives a Curie tail as $\chi_{\mathrm{im}}(T) = C/(T - \theta)$, and χ_0 is the temperature independent term. The $\chi_{\mathrm{BiVO}}(T)$ is given by a Bonner−Fisher equation, where g is an averaged g-factor, $X = kT/|J|$, J being the antiferromagnetic coupling constant between the nearest neighbors defined by $H_{ex} = J\sum_i S_iS_{i+1}$, p is a scaling constant, that is, molar fraction of magnetic V^{4+} ions which give rise to this 1D magnetism, and the values for the coefficients in the equation, $A_0 = 0.25$, $A_1 = 0.14995$, $A_2 = 0.30094$, $B_1 = 1.98620$, $B_2 = 0.68854$, and $B_3 = 6.06260$, are used in our fitting.[29,30] The fitting results, assuming $g = 2.0$, can be visualized from the solid lines in Figure 4. Clearly, this model proves to fit the magnetic susceptibility data very well in the whole temperature range of measurements. The values obtained for J/k, p, C (Curie constant), θ (Weiss temperature), and χ_0 are summarized in Table 1. The $\chi(T)$ curve of $Bi_{3.6}V_2O_{10}$ seems to be different

Table 1. Parameters Obtained in Fitting the Experimental Curve for Different Samples with Bonner Fisher Model

	J/k	p	C	θ	χ_0
$Bi_4V_2O_{10.6}$	55.8	0.282	0.00188	−2.8	-7.5×10^{-5}
$Bi_{3.87}V_2O_{10.4}$	56.5	0.299	0.00232	−6.5	-7.4×10^{-5}
$Bi_{3.6}V_2O_{10}$	53.1	0.291	0.00607	−4.2	-4.6×10^{-5}

from those of $Bi_4V_2O_{10.6}$ and $Bi_{3.87}V_2O_{10.4}$, the values of J/k and p, however, are essentially close between $Bi_{3.6}V_2O_{10}$ and the other two compounds, indicating all three compounds bear almost the same $\chi_{\mathrm{BiVO}}(T)$ part. This means all three representative samples are the same 1D magnetic chain systems. The values of p are approximately 30% for the three compounds, which is close to the ideal value of 33% for the A-type structure of $Bi_4V_2O_{10.66}$.

These results underline the $S = {}^1/_2$ 1D antiferromagnetic behavior common to three $Bi_4V_2O_{11-\delta}$ member compounds and indicate that V^{4+} ions have formed a linear spin chain structure in the host lattice, which exactly coincides with the proposed A-type structure from our Rietveled refinement, where $V^{4+}O_6$ octahedra are arranged in a 1D fashion. We can also derive the equally important information that the structure of the V−O layers is independent of oxygen stoichiometry, and the loss of oxygen from $\delta = 0.4$ to $\delta = 1$ can thus be accommodated only by creating oxygen vacancies in the Bi−O layers. In principle, this scenario is completely in accord with the presence of bismuth impurity whose precipitation would be at the cost of oxygen content.

3.3. Phase Transitions. Given the different allotropic forms the parent phase $Bi_4V_2O_{11}$ has exhibited as a function of temperature, there is a good reason for us to expect that the phase diagram for $Bi_{4-x}V_2O_{11-\delta}$ could also include rich polymorphs for each possible member compound. To detect the phase transition and resolve the temperature dependence of structures, both in situ high temperature XRD and DTA are employed for detailed measurements on selected samples. Prior to discussing these results, however, it should be emphasized here that all $Bi_4V_2O_{11-\delta}$ samples are strongly sensitive to oxygen at elevated temperatures. For example, a thermogravimetric measurement on a small portion of $Bi_{3.6}V_2O_{10}$ powders by heating to 800 °C in flowing helium gas of 99.9999% purity even saw serious oxidation behavior and weight gain (see Supporting Information, Figure S2). Hence, particular care has to be taken for the high temperature characterization of any samples in this system. All data in previous reports that rely on inert or reducing gas should be reconsidered carefully. Our approach in dealing with this problem is that all samples are sealed into evacuated thin-walled quartz capillaries and vessels for high temperature XRD and DTA measurements, respectively.

The first sample whose phase transition was monitored in situ by DTA is $Bi_4V_2O_{10.6}$ as it is the boundary phase in the structural region with A-type. Presented in Figure 5, the DTA

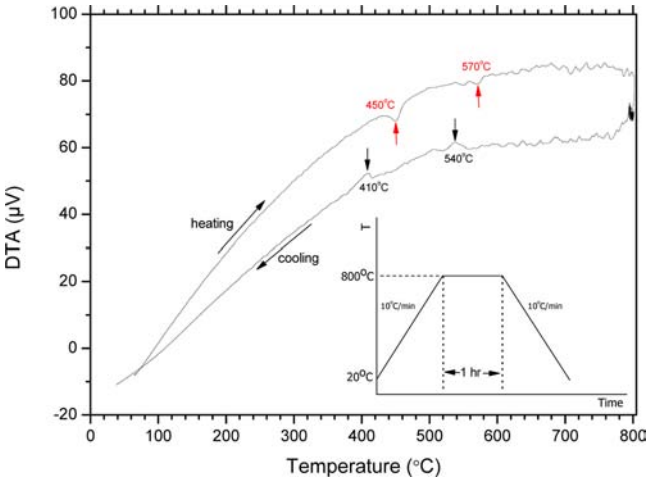

Figure 5. DTA on a $Bi_4V_2O_{10.6}$ powder sample which was sealed in an evacuated quartz vessel. The inset describes the thermal history of our measurement.

curve revealed two endothermic peaks at 450 and 570 °C on heating. On cooling two exothermic peaks appear at 540 and 410 °C with hysteresis. This observation indicates two consecutive and reversible phase transitions, and there are at least three allotropic forms in $Bi_4V_2O_{10.6}$. By analogy with $Bi_4V_2O_{11}$ we hereafter define the intermediate and high-temperature phases as B and C phases, respectively.

To further confirm these phase transitions as well as to probe structural details of different phases, in situ high temperature XRD was carried out on representative samples which were also sealed in evacuated capillaries. Figure 6 illustrates the development of the XRD patterns of $Bi_4V_2O_{10.6}$ as a function of temperature. With increasing temperature the XRD patterns recorded between 400 and 475 °C show a sudden shift of the (006) peak from around 35.7° in A-$Bi_4V_2O_{10.6}$ toward lower angle at 475 °C. Apart from the (006) shift, another major

dx.doi.org/10.1021/ic400111w | Inorg. Chem. 2013, 52, 5206−5213

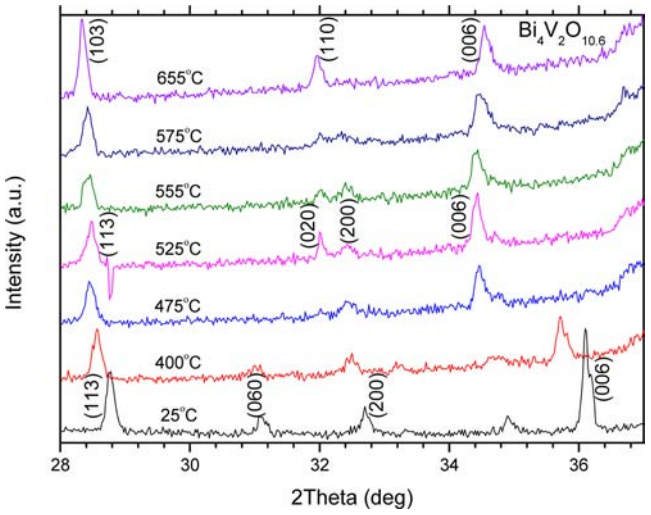

Figure 6. In situ XRD analysis shows the structural transformation of $Bi_4V_2O_{10.6}$ from oxygen vacancy ordered orthorhombic to disordered orthorhombic and finally into simple perovskite-type tetragonal. Because the samples are sealed into a quartz capillary, only diffraction peaks with relatively strong intensities are observable.

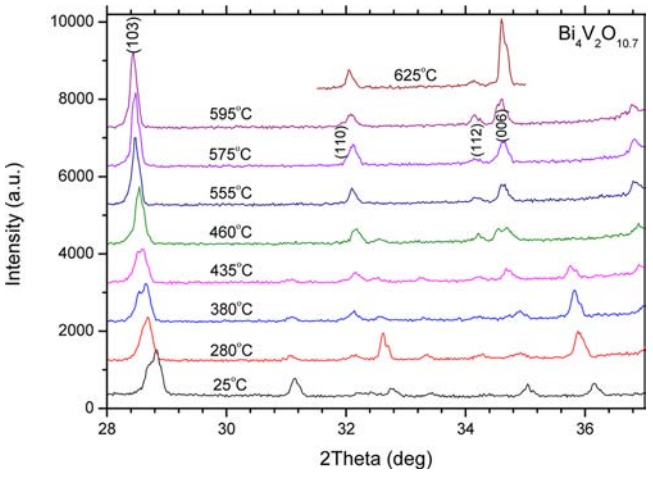

Figure 7. In situ XRD analysis shows the phase transition of $Bi_4V_2O_{10.7}$ from the phase mixture into a final single perovskite-type tetragonal compound.

change involves two reflections in the 2θ range of 30−34°. In combination with the DTA result, this phase transition between 400 and 475 °C is of first-order transition nature and can be attributed to the A→B transition. Moreover, the splitting of peaks (060) and (200) in the A-phase decreases significantly upon the formation of the B-phase, possibly implying a transition from an oxygen ordered structure to a disordered one. With the further rise in the temperature a single peak appears to replace the separated two peaks as shown in the XRD profiles for 655 °C. This kind of peak merging is widely observed when a new phase, the C-phase in the current case, with improved symmetry emerges. Added evidence is that applying the simple tetragonal perovskite γ-$Bi_4V_2O_{11}$ structure to C−$Bi_4V_2O_{10.6}$ yields a good match in indexing all observed reflections. The B-phase, on the other hand, can be indexed on the basis of an orthorhombic unit cell which is related to the C-phase by $\sqrt{2}a_C \times \sqrt{2}a_C \times c_C$, which corresponds to $GdFeO_3$-type distortion characteristic of a perovskite structure. That means (060) and (200) in the A-phase become (020) and (200), respectively, in the B-phase before proceeding to (110) in the C-phase finally. At this moment, it can be easily recognized that the C→B transition behaves differently from $\gamma \rightarrow \beta$, as the latter is known to be due to the ordering of oxygen vacancies whereas the former is driven by the tilting and rotation of VO_6 octahedra.

The above argument tends to force us to conclude that both C- and γ-phases are essentially the same in the structure. To clarify this hypothesis and fill in the higher temperature part of the phase diagram, a member phase $Bi_4V_2O_{10.7}$ in the two phase mixture region is selected as the second compound on which to perform in situ high temperature XRD experiments. At room temperature, the presence of both A- and α-phases is most clearly demonstrated in Figure 7 by the doublet around 2θ = 28.4−29.2° for the main peaks for two phases. Between 435 and 460 °C, the doublet merges into a single peak and the (006) peak around 36° inherent in A-phase disappears, indicating the A→B transition. It is difficult to detect the $\alpha \rightarrow \beta$ transition from in situ high temperature XRD because the super reflections characteristic of α- or β-phases have such weak intensity that they are hardly observed in XRD measurements using samples that were sealed into capillaries. However, we can conclude that the $\alpha \rightarrow \beta$ transition takes place around 440 °C, from the fact that the α-phase transforms to the β-phase at 440 °C in $Bi_4V_2O_{11}$. The peak merging around 2θ = 28.4−29.2° indicates a transition from the mixed phase to the uniform phase that is B−$Bi_4V_2O_{10.7}$. With the temperature continuing to rise, the diffraction pattern at 575 °C can be indexed according to the γ or C typed structure. We have known $\beta \rightarrow \gamma$ and B→C both to occur at around 570 °C.

In situ XRD analysis confirmed that $Bi_4V_2O_{11-\delta}$ has a wide nonstoichiometric range of at least $0 \leq \delta \leq 0.4$ in the high temperature region above 570 °C. On the other hand, one of the most important contributions of this study is that for the first time we have identified a wide oxygen nonstoichiometry regime $0.4 \leq \delta \leq 1$ for $Bi_{4-x}V_2O_{11-\delta}$ where the A-typed phase survives. A full phase diagram would thus call for collecting more in situ XRD data on other A-typed compositions. The δ = 0.6 and 1.0 samples were chosen for this experiment. For $Bi_4V_2O_{10.4}$ with Bi-precipitation, we found that the successive phase transitions of A→B and B→C take place around 450 and 570 °C, respectively. As for $Bi_{3.6}V_2O_{10}$, we found a reduced phase transition temperature for A→B, that is at 370 °C, and almost the same transition temperature of 570 °C for B→C.

On the basis of all data we have obtained from DTA and in situ XRD measurements on different compositions, we can construct a simple phase diagram for the $Bi_4V_2O_{11-\delta}$ ($0 \leq \delta \leq 1$) system as shown in Figure 8. Before looking further into the phase diagram of the current system, one important point has to be made clear that by focusing only on the composition range of $0 \leq \delta \leq 1$ in the present study it is by no means our intention to convey an assumption that there are no phases when $\delta > 1$. Studies over materials with large δ values, or in other word further reduced oxygen stoichiometry, will be the subject of a different paper. Here, the real phase transition temperature for $Bi_4V_2O_{10.9}$ in Figure 8 was not experimentally actually confirmed, and we artificially use the results for $Bi_4V_2O_{11}$ including $BiVO_4$ as an impurity, given the small disparity between the two phases. Furthermore, it should be noted that $Bi_4V_2O_{11-\delta}$ with $\delta > 0.4$ contain Bi metal as an impurity and therefore it should be expressed more precisely as $Bi_{4-x}V_2O_{11-\delta}$ with a relation of $x = 2\delta/3 - 4/15$.

dx.doi.org/10.1021/ic400111w | Inorg. Chem. 2013, 52, 5206−5213

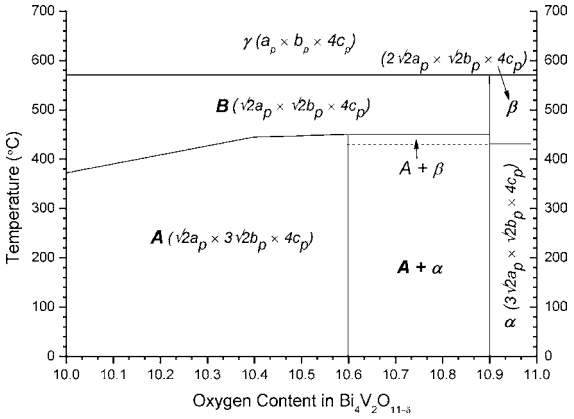

Figure 8. Phase diagram for the oxide system of $Bi_4V_2O_{11-\delta}$ ($0 \leq \delta \leq 1$). It should be noted that all phases in the compositional range of $Bi_4V_2O_{11-\delta}$ ($0.4 < \delta \leq 1$) coexist with bismuth, although the phase formation temperature for B and γ is significantly higher than the melting point of bismuth (272 °C), and it is difficult to probe the presence of liquid Bi through in situ XRD. The relationships of the crystallographic unit cells of the different phases are illustrated by comparison with the simple perovksite structural unit, $a_p \times b_p \times c_p$.

3.4. Discussion. Looking back at the whole $Bi_4V_2O_{11-\delta}$ system, with decreasing oxygen stoichiometry, compensating tetravalent vanadium is increasingly formed as would be expected in vanadium oxides where vanadium valence normally changes continuously; however, beyond $\delta = 0.4$, reduction was suddenly switched to the Bi site via precipitation of Bi metal and thus leaving oxygen vacancies in the Bi−O layer. This means that the energy cost to remove oxygen from the V−O layer beyond $\delta = 0.4$ is larger than that from the Bi−O layer. As a result, $V^{3+}/V^{4+} = 2/3$ is retained across the whole range of compositions with $0.4 \leq \delta \leq 1$. Such an unusually rigid vanadium pair in the presence of a reducing atmosphere is rarely observed in any other compounds. It may suggest a reducing limit, which is 2/3, for vanadium in the current system. In preliminary experiments, the A-type structure is retained beyond $\delta = 1$. It is very interesting to know why the structure with a larger amount of Bi and oxygen vacancies in the Bi−O layer is stable, in terms of defect chemistry, but this is a future work.

In light of our phase diagram, any composition in the current system will readily crystallize in γ-typed phase whose oxygen in the vanadate layer has been known to be highly disordered.[15] For instance, the observed oxygen anionic conductivity in γ-type $Bi_4V_2O_{11}$ is much higher than that of the most widely used oxygen conductor yttria-stabilized zirconia (YSZ).[13] In our case for the oxygen deficient member material, for example, γ-$Bi_{3.6}V_2O_{10}$, its increased oxygen vacancy without ordering is expected to further facilitate the ease of oxide ion hopping between the same crystallographic sites. Our preliminary neutron diffraction experiment on γ-$Bi_{3.6}V_2O_{10}$ also showed serious anisotropic oxygen displacement. Despite the sensitivity to oxidation which rules out the possibility for applications as oxygen electrolytes running in the ambient atmosphere, we may still depend on such materials for better access to the local mechanism of oxygen anionic conduction which is a key issue in renewable energy harvesting.

Our phase diagram also reveals that the uniform γ-phase (or C-phase) separates into the $\beta(\alpha)$- and A-phases. Such a phase separation is understandable because the $\beta(\alpha)$- and A-phases have different vacancy-ordered perovskite $VO_{4-\Delta}$ slabs with the stoichiometric compositions of $VO_{3.5}$ for the $\beta(\alpha)$-phase ($Bi_4V_2O_{10.9}$) and $VO_{3.33}$ for the A-phase ($Bi_4V_2O_{10.66}$).[14,20] An important question arises why one of the separated phases is not $Bi_4V_2O_{10.66}$ but $Bi_4V_2O_{10.6}$. This can be explained by allowing oxygen vacancy of $y = 0.03$ in the (Bi_2O_{2-y}) sheet, namely, the structure consists of $2(Bi_2O_{1.97})$ sheets and $2(VO_{3.33})$ perovskite slabs, giving the chemical formula $Bi_4V_2O_{10.6}$. If $Bi_4V_2O_{10.9}$ which is the other separated phase has the same $Bi_2O_{1.97}$ sheet, the composition of the V−O perovskite slab becomes $VO_{3.48}$ which is very close to the stoichiometric composition of $VO_{3.5}$ for the α-structure.

4. CONCLUSIONS

In summary, a full phase diagram for the $Bi_4V_2O_{11-\delta}$ ($0 \leq \delta \leq 1$) system is built for the first time based on the present detailed study by examining the whole spectrum of composition. One structure related to the established $Bi_4V_2O_{11}$ phase survives in a very narrow δ range whereas the other structure type with its parent phase $Bi_4V_2O_{10.6}$ shows unusual robustness from $\delta = 0.4$ until $\delta = 1$. Surprisingly, the decreasing oxygen stoichiometry in this structural region is found to be accommodated not by lowering the valence of vanadium as would be expected, but instead by reducing bismuth. It means the Bi site is favored over the V site upon reduction. This conclusion was further strengthened by the measurements of magnetic susceptibility over different compositions. All samples show the similar behavior that is characteristic of a 1D spin chain structure. The rigid V−O unit shared by all compositions between $\delta = 0.4$ and 1 is thus responsible for the robustness of the second type structure in the current phase diagram. In situ XRD investigations as a function of temperature provided strong evidence for the existence of three allotropic forms, which are α, β, and γ for the $Bi_4V_2O_{11}$ type and A, B, and γ for the $Bi_4V_2O_{10.6}$ type. When heated to 570 °C or higher temperature, all compositions become uniform by forming the same tetragonal γ phase. The γ-$Bi_4V_2O_{11}$ phase is well-known as an oxygen anionic conductor with exceptionally high ion mobility. With a larger amount of intrinsic disordered oxygen vacancies, γ-$Bi_4V_2O_{11-\delta}$ phases, particularly γ-$Bi_{3.6}V_2O_{10}$, hold great potential in offering optimized ionic conductivity. On the other hand, given the interesting bismuth chemistry and low dimensional magnetism, this oxygen deficient system provides a very unique opportunity for the study at the interplay between structure and property.

■ ASSOCIATED CONTENT

Ⓢ Supporting Information

Detailed phase transition data for $Bi_4V_2O_{11}$ and TG/DTA results for $Bi_{3.6}V_2O_{10}$ at elevated temperatures. This material is available free of charge via the Internet at http://pubs.acs.org.

■ AUTHOR INFORMATION

Corresponding Author

*E-mail: yqzhang@issp.u-tokyo.ac.jp.

Notes

The authors declare no competing financial interest.

■ ACKNOWLEDGMENTS

This work was supported by a Grant-in-Aid for Scientific Research (No. 22244041) from Japan Society for the Promotion of Science (JSPS).

REFERENCES

(1) Zhou, W. *J. Solid State Chem.* **1988**, *76*, 290−300.
(2) Zhou, W. *J. Solid State Chem.* **1990**, *87*, 44−54.
(3) Jo, W. J.; Jang, J. W.; Kong, K. J.; Kang, H. J.; Kim, J. Y.; Jun, H.; Parmar, K. P. S.; Lee, J. S. *Angew. Chem., Int. Ed.* **2012**, *51*, 3147−3151.
(4) Kuang, X. J.; Payne, J. L.; Johnson, M. R.; Evans, I. R. *Angew. Chem., Int. Ed.* **2012**, *51*, 690−694.
(5) Shantha, K.; Varma, K. B. R. *Solid State Ionics* **1997**, *99*, 225−231.
(6) Abraham, F.; Debreuille-Gresse, M. F.; Mairesse, G.; Nowogrocki, G. *Solid State Ionics* **1988**, *28*−*30*, 529−532.
(7) Abraham, F.; Boivin, J. C.; Mairesse, G.; Nowogrocki, G. *Solid State Ionics* **1990**, *40*−*41*, 934−937.
(8) Kim, N.; Clare, C. P. *Science* **2002**, *297*, 1317−1320.
(9) Zhang, Y. Q.; Su, Z. X.; Azad, A. K.; Zhou, W. Z.; Irvine, J. T. S. *Adv. Energy Mater.* **2012**, *2*, 316−321.
(10) Xie, K.; Zhang, Y. Q.; Meng, G. Y.; Irvine, J. T. S. *Energy Environ. Sci.* **2011**, *4*, 2218−2222.
(11) Fleming, W. J. *J. Electrochem. Soc.* **1977**, *124*, 21−28.
(12) Seong, S.; Yee, K. A.; Albright, T. A. *J. Am. Chem. Soc.* **1993**, *115*, 1981−1987.
(13) Goodenough, J. B. *Annu. Rev. Mater. Res.* **2003**, *33*, 91−128.
(14) Mairesse, G.; Roussel, P.; Vannier, R. N.; Anne, M.; Nowogrocki, G. *Solid State Sci.* **2003**, *5*, 861−869.
(15) Mairesse, G.; Roussel, P.; Vannier, R. N.; Anne, M.; Pirovano, C.; Nowogrocki, G. *Solid State Sci.* **2003**, *5*, 851−859.
(16) Joubert, O.; Jouanneaux, A.; Ganne, M. *Mater. Res. Bull.* **1994**, *29*, 175−184.
(17) Abrahams, I.; Krok, F. *J. Mater. Chem.* **2002**, *12*, 3351−3362.
(18) Abrahams, I.; Bush, A. J.; Krok, F.; Hawkes, G. E.; Sales, K. D.; Thornton, P.; Bogusz, W. *J. Mater. Chem.* **1998**, *8*, 1213−1217.
(19) Huve, M.; Vannier, R. N.; Nowogrocki, G.; Mairesse, G.; Tendeloo, G. V. *J. Mater. Chem.* **1996**, *6*, 1339−1345.
(20) Joubert, O.; Jouanneaus, A.; Ganne, M. *Nucl. Instrum. Methods Phys. Res., Sect. B* **1995**, *97*, 119−122.
(21) Millan, P.; Rojo, J. M.; Castro, A. *Mater. Res. Bull.* **2000**, *35*, 835−845.
(22) Satto, C.; Millet, P.; Sciau, P.; Roucau, C.; Galy, J. *Mater. Res. Bull.* **1999**, *34*, 655−664.
(23) Ueda, Y. *Chem. Mater.* **1998**, *10*, 2653−2664.
(24) Mizoguchi, H.; Matsuishi, S.; Hirano, M.; Tachibana, M.; Takayama-Muromachi, E.; Kawaji, H.; Hosono, H. *Phys. Rev. Lett.* **2011**, *106*, 057002.
(25) Lee, P. A.; Nagaosa, N.; Wen, X. G. *Rev. Mod. Phys.* **2006**, *78*, 17−85.
(26) Kamihara, Y.; Watanabe, T.; Hirano, M.; Hosono, H. *J. Am. Chem. Soc.* **2008**, *130*, 3296−3297.
(27) Larson, A. C.; Von Dreele, R. B. *General Structure Analysis System (GSAS)*; Los Alamos National Laboratory Report LAUR; Los Alamos National Laboratory: Los Alamos, NM, 2004; pp 86−748.
(28) Toby, B. H. *J. Appl. Crystallogr.* **2001**, *34*, 210−213.
(29) Isobe, M.; Ueda, Y. *J. Phys. Soc. Jpn.* **1996**, *65*, 1178−1181.
(30) Hatfield, W. E. *J. Appl. Phys.* **1981**, *52*, 1985−1990.